City Research Online

City, University of London Institutional Repository

**Citation:** Massart, P. F. R., Dhanisetty, V. S. V., Kassapoglou, C., Verhagen, W. J. C. W. & Curran, R. (2020). Deducing the physical characteristics of an impactor from the resultant damage on aircraft structures. International Journal of Solids and Structures, 200-201, pp. 94-105. doi: 10.1016/j.ijsolstr.2020.05.017

This is the published version of the paper.

This version of the publication may differ from the final published version.

**Permanent repository link:** https://openaccess.city.ac.uk/id/eprint/31795/

**Link to published version:** https://doi.org/10.1016/j.ijsolstr.2020.05.017

**Copyright:** City Research Online aims to make research outputs of City, University of London available to a wider audience. Copyright and Moral Rights remain with the author(s) and/or copyright holders. URLs from City Research Online may be freely distributed and linked to.

**Reuse:** Copies of full items can be used for personal research or study, educational, or not-for-profit purposes without prior permission or charge. Provided that the authors, title and full bibliographic details are credited, a hyperlink and/or URL is given for the original metadata page and the content is not changed in any way.

City Research Online: http://openaccess.city.ac.uk/ publications@city.ac.uk

International Journal of Solids and Structures 200–201 (2020) 94–105

Contents lists available at ScienceDirect

International Journal of Solids and Structures

journal homepage: www.elsevier.com/locate/ijsolstr

# Deducing the physical characteristics of an impactor from the resultant damage on aircraft structures

Philippe F.R. Massart, V.S. Viswanath Dhanisetty *, Christos Kassapoglou, W.J.C. (Wim) Verhagen, Richard Curran

*Faculty of Aerospace Engineering, Delft University of Technology, Kluyverweg 1, Delft 2619 HS, The Netherlands*

ARTICLE INFO

*Article history:*
Received 25 October 2019
Received in revised form 15 April 2020
Accepted 12 May 2020
Available online 23 May 2020

*Keywords:*
Structural impact
Dents
Aluminium fuselage
Damage modelling
Aircraft maintenance
Impact damage
Damage impactors

ABSTRACT

This paper proposes an analytical model that uses historical damage dimension data to deduce physical impactor characteristics (size and energy) that has caused a certain resulting damage. Maintenance tasks occur in operations due to impact, however the source of the damage caused in the event remains in most cases unknown. Consequently, by inferring what has caused a certain type of damage from the distribution of the damage type and severity relative to impactor types, maintainers can be better prepared in terms of what to expect from a given impactor source. The developed model introduces a novel transition deformation region between the local deformation and the global plate deflection, allowing for fast and accurate predictions of the impact event. Using the known aluminium structural properties and damage dimensions, the damage data is converted into impactor data. The model is applied in a case study using 120 fuselage dent damages dimensions (length, width, and depth) from a Boeing 777 fleet. The results show that the model deduces impactor characteristics for 94% of the considered damages, ranging up to 240 J and 110 mm for impactor energy and radius respectively.
© 2021 The Authors. Published by Elsevier Ltd. This is an open access article under the CC BY license (http://creativecommons.org/licenses/by/4.0/).

## 1. Introduction

Airworthiness, in terms of the external structure (fuselage and wing skin), is challenged daily by damage occurrence caused by impact events. In addition to airworthiness and safety issues, airlines are continually challenged by maintenance decision-making (Dhanisetty et al., 2019; Dhanisetty et al., 2017) and the associated cost and downtime which affects maintenance cost and aircraft/fleet availability and Direct Operating Cost (Curran et al., 2002; Curran et al., 2003; Curran et al., 2007). Current state-of-the-art considers impact damage and the effect it has on aircraft maintenance, as demonstrated by Chen et al. showing that impacts cause more than 50% of all aircraft structural damage such as dents, delamination and holes (Chen et al., 2014). These types of damage vary in size (diameter and depth) (Chen et al., 2014), requiring temporary or permanent repairs based on severity. By extension the sources of these damages can be just as varied in terms of type (runway debris, tool drops, ground service equipment or wildlife) and energy of impactor (Soldatini et al., 2010; Martin et al., 2011; Shupikov et al., 2012; Honomichl et al., 2013; Chen et al., 2011; Federal Aviation Administration, 2010). Identifying the impactors from historical damage dimensions will benefit aircraft operators and Maintenance, Repair and Overhaul (MRO) organisations, by shifting the viewpoint away from damage and towards the actual origin/source of the impact event. Thereby mitigation plans can be proactive in preventing impactors that cause unplanned repairs and achieve higher up-time of aircraft with less annual maintenance cost. In addition, extensive historical data from metal aircraft can be used to identify potential threats for composite aircraft for which there is much less service history.

Federal Aviation Administration (FAA) have conducted surveys to capture the variability of non-wildlife impactor material type and size (Federal Aviation Administration, 2010). Such surveys of hazardous debris around an aircraft can find a collection of potential impact threats, but the relation between impactor and the resulting damage is unknown because human inspectors can only observe the final resultant damage. Therefore, to understand the types of impactors that would strike an aircraft, this paper proposes that, given the impactor material, the characteristics ($R_i$, radius and $U_i$, energy) can be deduced from a set of structural damage dimensions and material properties of the damaged structure. The focus of the present work is attributed to low-speed impact damage which covers tool and equipment drops, walk traffic during maintenance, luggage drops, and some ground collisions. These correspond to the majority of reported impact events in service.

* Corresponding author.
*E-mail address:* v.s.v.dhanisetty@tudelft.nl (V.S.V. Dhanisetty).

https://doi.org/10.1016/j.ijsolstr.2020.05.017
0020-7683/© 2021 The Authors. Published by Elsevier Ltd.
This is an open access article under the CC BY license (http://creativecommons.org/licenses/by/4.0/).

For low speed impact, where stress waves have not reached the boundary, the impact event can be treated as quasi-static with the boundary conditions affecting only the global deformation of the plate as computed by a quasi-static analysis. It is recognised that there are various criteria for determining whether an impact event is quasi-static which are not only dependent on mass Olsson, 2000, see for example (Swanson, 1992). Here, the model focuses on response dominated by structural deflections as those characterised by large mass impacts. To execute the process of predicting impactors from damage dimensions, an analytical model has been developed called Modelling Impact Damage on Metal Aircraft Structures (MIDAS-M).

The modelling process of MIDAS-M is defined in two steps. First, for a given impactor an impact event is approximated, and the corresponding damage (i.e., a permanent dent) is estimated. Second, the analytical model is reverse engineered to deduce the impactor characteristics (radius and energy) from the permanent damage as an input. These two steps are respectively referred to as the inductive problem (i.e. determine the damage) and deductive problem (i.e. estimate the impactor). To the best of the authors' knowledge, methods found in literature solely focus on the inductive problem (Simonsen and Lauridsen, 2000; Abrate, 2001; Davies and Olsson, 2004; Lee et al., 2004), while the deductive problem is not explicitly addressed.

This paper differentiates itself from earlier work on metal structure impacts in regards to the assumed mode of deformation: where earlier works superimposed the local deformation on the global deflection (Shivakumar et al., 1983; Abrate, 2001), MIDAS-M considers an additional 'transition' region between the local and global deformation modes. As a result, the deformation shape of the plate during an impact is more realistically modelled.

Furthermore, the analytical model MIDAS-M has been verified using a finite element model (FEM), which is validated by experimental results from Fagerholt et al. (2010). By comparing specific impact cases with the analytical model and the computational model, the MIDAS-M range of applicability is determined.

## 2. Development of MIDAS-M for metal plates

The structural response of metals during an impact has been explored by various researchers in literature (Abrate, 2001; Yigit and Christoforou, 2007; Singh and Mahajan, 2016; Davies and Zhang, 1993; Esrail and Kassapoglou, 2014; Jones, 2011; Langseth and Larsen, 1988; Langseth and Larsen, 1990; Langseth and Larsen, 1994). MIDAS-M model has been developed to address some gaps in modelling the different modes of deformations for impact damages on metal plates.

### 2.1. Plate deformation and key assumptions

The key assumptions regarding the type of impact event and shape of plate during impact, scope the model development. These assumptions help define the modes of deformations to be modelled in MIDAS-M.

#### 2.1.1. Type of impact event

Within literature, a variety of methods have been used to model impact responses. Depending on the type of impact event, researchers have emphasised different aspects of the structural response (Abrate, 2001; Yigit and Christoforou, 2007; Singh and Mahajan, 2016; Davies and Zhang, 1993; Esrail and Kassapoglou, 2014; Mittal, 1987; Schonberg et al., 1987; Langseth and Larsen, 1994; Langseth and Larsen, 1990). However, it is generally agreed that an impact response consists of both a structural deflection and local deformation. In addition to material effects, the local behaviour is often seen as both boundary- and time-independent, whereas the global response's boundary- and time-dependency is influenced by the type of impact event (Cantwell and Morton, 1991; Richardson and Wisheart, 1996; Abrate, 1994; N. Razali et al., 2014; Davies and Olsson, 2004). For example, Olsson (2000) defines a mass criterion to distinguish boundary dependent and independent events, whereas (Cantwell and Morton, 1991; Richardson and Wisheart, 1996; and Abrate, 1994) use various velocity regimes to define different types of impact. Within this study, the following is assumed in the development of MIDAS-M:

*The impact event is a quasi-static event.*

#### 2.1.2. Shape of plate

Another key assumption that influences the development of the proposed analytical model is the shape of plate:

*The structural deformation consists of the three distinct regions: local deformation, transition, and plate deflection.*

These three regions are illustrated in Part (b) of Fig. 1, which includes an alternative local contact model based on penetration limits, and consecutively the interaction with, and transition to a global plate deflection.

#### 2.1.3. Mode of deformation

Within literature, contact or impact on metallic structures is generally approached by two different methods: either based on contact laws or penetration limits. On the one hand, contact laws are based on deformations within the contact area (i.e. $r < R_c$), whereas penetration limits focus on the region outside the contact area (i.e. $r \geqslant R_c$). The local contact laws are often modifications of the elastic theory of Hertz. These modifications are intended to capture the changes in stiffness due to plasticity. Cairns and Simple (1991) therefore proposes an elasto-plastic model, while Big-Alabo et al. (2015) argue that a four-step (elastic, bi-elasto-plastic and fully plastic) model is more applicable. In an earlier study, Chen and Engel (1972) studied how the contact stresses change as a function of plate stiffness and thickness. However, these contact laws are developed by assuming that the target is an elastic half-space or has a rigid foundation. The global deformation of flexible targets is typically superimposed, but the deformation behaviour outside the contact area is thereby neglected. Experiments as reported by both Fagerholt et al. (2010) and Mohotti et al. (2013), however, indicate that deformation behaviour of steel and aluminium targets upon impact is dominated by the region outside the contact area. This is also shown by their reported residual deformation radii, which are larger than the indentor radii. Penetration limit approaches focus on this outer region, and are intended for flexible or deformable targets.

By combining the penetration limit methods of Simonsen and Lauridsen (2000) and Lee et al. (2004), with the conventional interaction of local and global deformations using a Lumped Parametric Model (LPM) (Abrate, 2001; Shivakumar et al., 1983) (Fig. 2), MIDAS-M attempts to model deformation over a wider range of impact energies.

### 2.2. Loading phase

MIDAS-M introduces a novel transition region within the theoretical superposition of local deformation and plate deflection. The transition region combines the contribution of membrane approach and plate deflection theory to obtain a more realistic deformation shape. The loading phase and the interaction of the different contributions are detailed in this section.

#### 2.2.1. Contact model

Penetration of metal plates typically occurs at impactor displacements ($\delta$) significantly larger than the plate thickness ($t$)

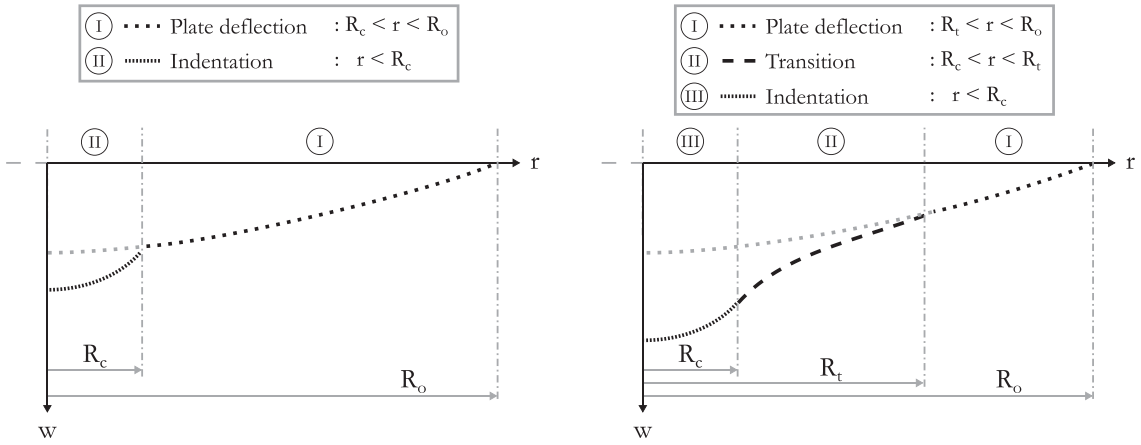


(a) Conventional deflection as used by Shivakumar et al. [18]

(b) Assumed deflection shape in MIDAS-M

**Fig. 1.** Differences in assumed deflection shapes.

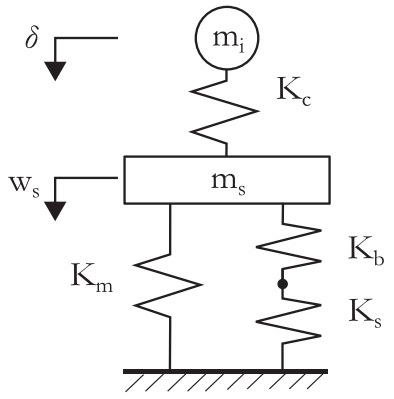


**Fig. 2.** Simplification of structural response of boundary dependent impact in a two lumped parameter system (Abrate, 2001; Shivakumar et al., 1983).

(Lee et al., 2004). Both Lee et al. (2004) and Mohotti et al. (2013) have shown that at these large deflections membrane strains dominate around the contact region. Both Simonsen and Lauridsen (2000) and Lee et al. (2004) developed an axi-symmetric theoretical model based on a clamped circular plate ($R_0$) indented in the centre with a spherical impactor ($R_i$), as shown in Fig. 3. The plate wraps around the punch and exhibits a pure tensile (membrane)

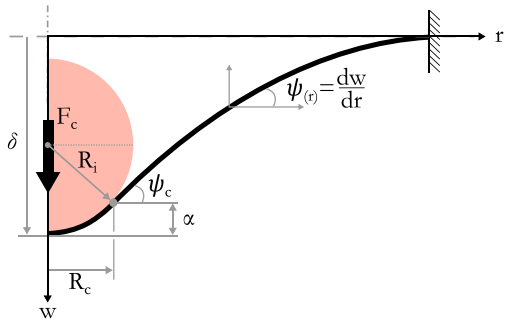


**Fig. 3.** Definition of loading state of plate during quasi-static deformation (modified from Lee et al., 2004).

stress ($\sigma_{rr}$) outside the contact area. This defines the vertical equilibrium as:

$$\begin{aligned} F_c &= 2\pi r\, t\sigma_{rr}\ \sin\psi(r) \\ &= 2\pi r\, C_0 t_0\ \left[\tfrac{1}{2}\sin^2\psi(r)\right]^n \cos\psi(r)\ \sin\psi(r),\ r \in (R_c, R_0) \\ \text{with}\quad \sigma_{rr(r)} &= C_0\varepsilon_{rr}^n \\ \varepsilon_{rr} &= \tfrac{1}{2}\sin^2\psi \\ t_0 &= t\cos\psi(r) \end{aligned} \tag{1}$$

in which $\psi$ represents the deflection angle of the plate as function of distance ($r$) to the impact centre. Yielding of the material is accounted by a power hardening law, which depends on the strength coefficient ($C_0$) and work hardening exponent ($n$). The Almansi strain tensor is used to approximate the radial strain ($\varepsilon_{rr}$). This approximation, which differs from both Lee et al. (2004) (logarithmic strain) and Simonsen and Lauridsen (2000) (Green strain), is based on finite element simulations of Liu et al. (2014). The contact force as a function of local deflection ($\alpha$) is obtained from the force equilibrium by substitution of the known contact radius ($R_c$) and contact angle ($\psi_c = \psi_{(r=R_c)}$). This reference point allows solving for the deflection angle of the remainder of the plate by Eq. (2). In addition, for the indicated clamped circular plate, the corresponding displacement is determined by Eq. (3) (Simonsen and Lauridsen, 2000). The penetration limit ($\psi_{c,f}$), as defined by Liu et al. (2014), follows from the peak of the force displacement curve (i.e $\frac{\partial F_c}{\partial \psi_c} = 0$).

$$\frac{r}{R_i} = \frac{\left[\tfrac{1}{2}\sin^2\psi_c\right]^n \cos\psi_c\ \sin^2\psi_c}{\left[\tfrac{1}{2}\sin^2\psi(r)\right]^n \cos\psi(r)\ \sin\psi(r)} \qquad \text{with} \quad \cos\psi_c = 1 - \frac{\alpha}{R_i} \tag{2}$$

$$\delta = \alpha + \int_{R_c}^{R_0} \sin\psi(r)(r,\alpha)dr \tag{3}$$

$$\cos\psi_{c,f} = \sqrt{\frac{1}{3+2n}} \tag{4}$$

The procedure just described approximates the deformation state of the entire plate close to penetration, assuming pure membrane stains and clamped boundary conditions. MIDAS-M, however, should approximate the entire impact event, which includes bending strains further away from penetration state. In addition, the deformation shape is highly dependent on the geometry and

support conditions of the structure. It is assumed that the described behaviour in close vicinity of the point of contact can be assumed to be valid independent of the boundary conditions, whereas the dependency on boundary conditions further away from the point of contact needs to be defined.

*2.2.2. Interaction plate deflection and deformation due to contact*

The interaction between the local and global impact response is typically described by a LPM, as shown in Fig. 2. Local deformations can be neglected in most quasi-static impact cases. The relative magnitude of "contact" and "structural" stiffness can be assessed with diagrams such as the one proposed by Christoforou et al. (2012). The lower half of the LPM describes the global structural response, whereas the top refers to the local deformation. Both deformation contributions are effectively superimposed on each other. This results in the following energy equilibrium and force equivalence:

$$\frac{1}{2}m_i v^2 = E_m + E_{bs} + E_c \tag{5}$$

$$F_c = F_m + F_{bs} \tag{6}$$

The deformation resistance of the structure consists of contact, membrane, and combined shear and bending contributions (indicated by the subscripts $c, m$ and $bs$ respectively). The distinction between $m$ and $bs$ in the lower half of the LPM relates to the bending dominating behaviour at small deflections ($w_s < t$), compared to membrane behaviour at large deflections ($w_s > t$). The shear deformations are typically neglected for thin plates, which are the primary focus in this research. This relates to the shear stiffness ($K_s$) being significantly larger than the bending stiffness ($K_b$). The resulting dominating behaviour can be seen in Eq. (8) and (7) describing the force- and energy-deflection of the structure (Shivakumar et al., 1983; Olsson, 2015).

$$E_b + E_m = \int_0^{w_s} F_b + F_m \, dw_s = \frac{1}{2}K_b w_s^2 + \frac{1}{4}K_m w_s^4. \tag{7}$$

$$F_b + F_m = K_b w_s + K_m w_s^3, \tag{8}$$

The definitions of the respective stiffness terms are dependent on various structural properties, such as geometry and support structures. Within this research, the target structure is assumed to be a flat rectangular plate, which is either clamped or simply supported on all sides (indicated by subscripts *SS* and *CC* respectively). The definitions of $K_b$ and $K_m$, as given by Shivakumar et al. (1983) for circular plates, are summarised in Table 1.

**Table 1**
Definition of bending and membrane stiffness of a centrally loaded circular flat plate* (Shivakumar et al., 1983).

| Boundary Conditions (BC) | Bending Stiffness $\left(K_b^{CP}\right)$ | Membrane Stiffness $\left(K_m^{CP}\right)$ |
|---|---|---|
| Clamped (CC) | $\frac{4\pi E_r t^3}{3(1-\nu_r^2)R_0^2}$ | $\frac{\pi E_r t}{648 R_0^2}$ |
| Simply Supported (SS) | $\frac{4\pi E_r t^3}{3(3+\nu_r)(1-\nu_r)R_0^2}$ | $\frac{\pi E_r t}{R_0^2(3+\nu_r)^4}\left[\frac{191}{648}(1+\nu_r)^4 + \frac{41}{27}(1+\nu_r)^3 + \frac{32}{9}(1+\nu_r)^2 + \frac{40}{9}(1+\nu_r) + \frac{8}{3}\right]$ |

* $E_r$ and $\nu_r$ are the Young's modulus and Poisson ratio.
** Based on circular plates with radius $R_0$, but applicable to rectangular plates using an inscribed circle.

The membrane stiffness terms have been used consistently to be applicable for rectangular plates (Abrate, 1991; Abrate, 2001; Olsson, 2015; Christoforou, 2001). Alternatively, the bending stiffness of simply supported flat square plates can be obtained from plate deflection theory (Eq. (9) and (10) (Kassapoglou, 2013; Olsson, 2015)).

$$w_{s,SS\,(x,y)} = \frac{4F_c}{ab}\sum_m\sum_n \frac{\sin\frac{m\pi x}{a}\sin\frac{n\pi y}{b}}{D\left[\left(\frac{m\pi}{a}\right)^2 + \left(\frac{n\pi}{b}\right)^2\right]^2} \tag{9}$$

$$K_{b,SS}^{PT} = \frac{F_c}{w_{s,SS}(x=\frac{a}{2}, y=\frac{b}{2})} \tag{10}$$

with $a, b, F$ and $D$ being respectively the plate width, length, applied force and the bending rigidity. Comparison between the circular plate (*CP*) and the plate theory (*PT*) stiffness approximation shows differences as large as 10%. A similar trend is expected for clamped supports. The bending stiffness for clamped square plates ($K_{b,CC}$) is therefore adjusted using Eq. (11). The global deflection shape of a clamped plate is approximated by Eq. (12), using the resulting clamped bending stiffness and an assumed trigonometric deflection shape (Taylor and Govindjee, 2002).

$$K_{b,CC} = K_{b,CC}^{CP}\left(\frac{K_{b,SS}^{PT}}{K_{b,SS}^{CP}}\right) \tag{11}$$

$$w_{s,CC\,(x,y)} = \frac{F}{4}\frac{K_{b,CC}}{}\left(1-\cos\frac{2\pi x}{a}\right)\left(1-\cos\frac{2\pi y}{b}\right) \tag{12}$$

It is recognised here that the approximation of Eqs. 11 12, while within 10% for square plates, can be very inaccurate for rectangular plates with aspect ratios $> 1.2$. However, in such cases, using an equivalent circular plate with a radius given by Eq. (13) provides exactly the same deflection as a rectangular plate with dimensions $a$ and $b$.

$$R = a\sqrt{\frac{32}{\pi^3}\frac{a}{b}\frac{2+2\nu}{3+\nu}}\sum\sum\frac{sin\frac{m\pi}{2}sin\frac{n\pi}{2}}{\left[m^2+\left(n\frac{a}{b}\right)^2\right]^2} \tag{13}$$

It should also be pointed out that Eq. (10) refers to bending deflections and is obtained using small deflection theory. The plate behaviour is dominated by membrane effects, as shown in subsequent sections herein where both plasticity and large deflections are included. Thus, the effect of this small deflection approximation is expected to be small.

*2.2.3. Transition of plate deflection to local deformation*

The assumed deformation shape within MIDAS-M consists of three regions, as shown in Fig. 4. The local deformation follows from the geometric shape of the impactor (given by Eq. (14a)), and the global deflection (without local deformation) is given by Eq. (14c). The transition region between the local and global responses allows a more accurate combination of membrane and bending effects during plate deformation. The deformation within the transition region is defined by the integration of the event's deflection angle (i.e $\psi_e = \frac{\partial w_e}{\partial r}$) as given in Eq. (14b).

$$w_e(r) = \begin{cases} I & w_s(r) & \text{for} \quad R_t < r < R_0 & (a) \\ II & w_s(R_t) + \int_{R_t}^{r} \sin\psi_e(r)\, dr & \text{for} \quad R_c < r < R_t & (b) \\ III & w_e(R_c) + R_i - \sqrt{R_i^2 - r^2} & \text{for} \quad r < R_c & (c) \end{cases} \tag{14}$$

The deflection angle within the transition region is yet to be defined. The contact and global deflection approximations, described in Section 2.2.1 and 2.2.2, are essentially limit case solutions for the transition region, illustrated in Fig. 4. These cases refer to either a complete membrane or bending state of loading, while a

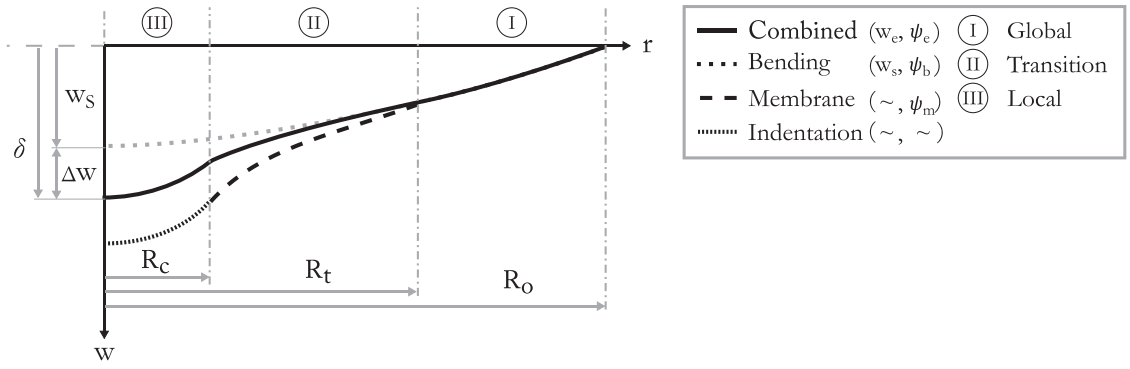


**Fig. 4.** The combined plate deflection based on weighted average of bending and membrane limit case solutions.

combination of both is present during an impact event. The resulting plate deformation, illustrated in Fig. 4 as the line labelled 'Combined', is effectively a weighted average of these limit cases. The respective weights are the relative force contributions given by the bending/membrane interaction in the LPM.

$$\psi_e(r) = \psi_b(r)\,\frac{F_m}{F_c} + \psi_m(r)\frac{F_b}{F_c} \tag{15}$$

in which $\psi_m(r)$ and $\psi_b(r)$ are the deflection angles of both limit cases. These angles follow from the penetration limit approach in Eq. (2) and the derivatives of the global plates deflection (i.e $\frac{\partial w_s}{\partial r}$ where $w_s$ is given by either Eqs. (9) or (12)). The transition point ($R_t$) is defined as the intersection of the deflection angle of both limit cases (i.e $\psi_m(r) = \psi_b(r)$).

The resulting deflection allows one to solve for the contact energy, which can be seen as additional work of the contact force over the relative displacement ($\Delta w$) between the plate bending deflection ($w_s$) and the impactor displacement($\delta$):

$$E_c = \int_0^{\Delta w} F_c\, d\,\Delta w \qquad \text{with} \quad \Delta w = \delta - w_{s(r=0)}. \tag{16}$$

The definitions of local and global impact of the plates allows solving the loading phase of the impact event, using Eq. (5).

### 2.3. Unloading phase – Permanent dent creation

The goal of the unloading phase is to obtain the residual dent by quantifying both the elastic and plastic deformation contributions. These contributions follow from the strain distribution of the plate, which is defined as solution for:

$$\varepsilon(r) = \varepsilon_m(r) + \varepsilon_b(r) \tag{17a}$$

$$\varepsilon_m(r) = \frac{1}{2}\sin\left(\frac{dw}{dr}\right)^2 \tag{17b}$$

$$\varepsilon_b(r) = -z\frac{d^2w}{d^2r} \tag{17c}$$

where $\varepsilon_b, \varepsilon_m$ and $z$ respectively refer to the bending, membrane strains and distance to the neutral axis. The plastic portion of the strains cause the residual dent, while elastic strains are assumed to restore to the original geometry. The plastic radius ($R_p$) is obtained by solving Eq. (17a)a for the yield strain ($\varepsilon_y$). The resulting residual deflection ($w_p$) is given by

$$w_p(r) = \begin{cases} w_e(r) - (R_p - r)\tan\left(\psi_{e(r)}\right) & \text{for} \quad R_c < r < R_p \quad (a) \\ w_p(R_c) + R^* - \sqrt{R^{*2} - r^2} & \text{for} \quad r < R_c \quad (b) \end{cases} \tag{17d}$$

in which Equation (17e) defines the relaxed impactor radius ($R^*$). This relaxed radius is a consequence of the relaxation of the dent, while the permanent dent radius remains constant.

$$R^* = \frac{R_c}{\sin\psi_p(R_p)}. \tag{17e}$$

## 3. Set-up of FEM to verify MIDAS-M

A Finite Element Model (FEM) is developed to evaluate the applicability of MIDAS-M. The accuracy of the FEM is verified with experimental results obtained from literature. Thereby, the FEM will represent a generalised realistic depiction of impact events against which the performance of MIDAS-M is compared.

### 3.1. General model

The model is developed using the commercially available finite element program Abaqus. The general model consists of two parts: the impactor and the impacted structure (respectively referred to as punch and target). The punch is modelled as a *Discrete Rigid Surface* using 3D bi-linear rigid 4-node quadrilateral elements (R3D4). The impactor mass and impact velocity are assigned to a reference point at the punch's centre of mass, which is rigidly constrained to its surface. The reference point is only allowed to move perpendicular to the target surface. The target is modelled as a *Deformable Solid*, using 8-node linear brick elements with reduced integration (C3D8R). *Enhanced Hourglassing Control* is applied to minimise uncontrolled element distortions, which could occur due to zero strains at the single integration point of C3D8R elements (Systèmes, 2013). The contact behaviour is modelled using Abaqus' General Contact algorithm including both tangential and normal contact behaviour. A penalty friction formulation is applied to the tangential behaviour using a friction coefficient of 0.15, while hard contact is enforced in the normal direction. This allows separation after contact but restricts penetration of the surface nodes (Systèmes, 2013). It should be noted that different friction coefficient values from almost 0 to 2 were examined and found to have negligible effect on the artificial strain energy (biggest change less than 4%) and maximum displacement (biggest change less than 0.15%). The constitutive behaviour of metals is modelled using a bi-linear stress-strain relation using the material's yield and ultimate strength (in terms of engineering stress and strain). The use of true stress and strain in a Johnson-Cook material model showed less than 1% difference from the bi-linear model for the cases studied here. This is shown as a function of mesh size for one of the cases in Fig. 5. The intended goal of the computational model is to compare deformation characteristics for low-velocity impact

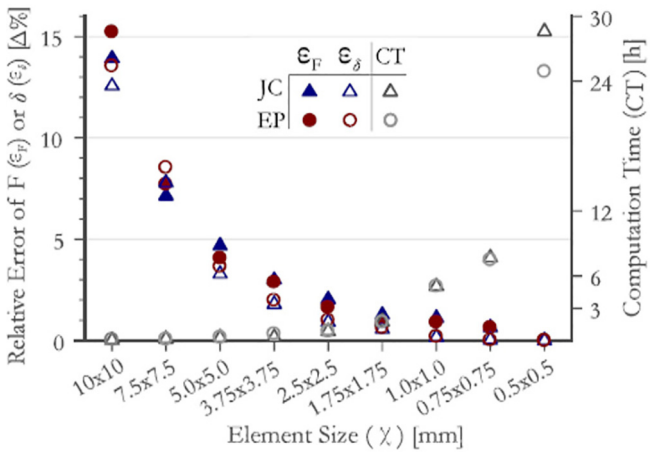


**Fig. 5.** (LHS) Relative error of displacement/force and (RHS) Computation time versus element size.

events, in which perforation does not typically occur. Damage characteristics and corresponding element deletion settings are therefore not considered. The dynamic nature of the impact event is modelled using Abaqus' Dynamic/Explicit step. The explicit direct integration procedure applies an automatic time incrementation scheme using a global estimator to determine stable time increments (Systèmes, 2013).

### 3.2. Dimensional and geometry dependent model characteristics

The reference results and MIDAS-M concern centrally impacted rectangular or circular flat plates that are either clamped or simply supported. This allows stimulating only a quarter of the model. The target plates consist of a free moving surface and a boundary region. Symmetry conditions are enforced on the inner boundaries of both regions, and the boundary region is constrained depending on the support condition (i.e. simply supported or clamped). As a result, either only the displacement or both displacement and rotational degrees of freedom of the respective nodes are fixed. A uniform meshing strategy is employed using element sizes of respectively 0.5 mm and 1.0 mm in the thickness and in-plane directions (indicated with subscripts $t$ and $n$). The in-plane element size follows from a mesh convergence, as described in Section 3.3.1. Fig. 6 shows the FEM models for two different impact scenarios. These correspond to meshes for either a clamped circular or a simply supported square plate used in respectively the comparison with experimental results and the verification of MIDAS-M.

### 3.3. Comparison computational model with literature results

The validity of the FEM is determined based on experimental results found in literature. Fagerholt et al. (2010) reported a study dedicated to the out-of-plane deformation measurements of AA5083-H116 plates subject to impact at three different velocities (i.e. 7.31, 7.92 and 10.69 m/s). In comparison to the assumed spherical impactor in MIDAS-M, Fagerholt et al. (2010) used a 30 mm diameter steel hardened blunt-nose projectile of 19.0 kg. The target plate consisted of 5 mm thick square plate with sides of 600 mm, which was mounted between two steel rings with an inner diameter of 500 mm. The relevant material properties of AA5083-H116 are summarised in Table 2.

#### 3.3.1. Mesh convergence of FEM

The reference case of 7.31 m/s is used to perform a mesh convergence. The convergence of the FEM is based on the relative error of the maximum displacement $\varepsilon_\delta$ and force $\varepsilon_F$, which is defined as

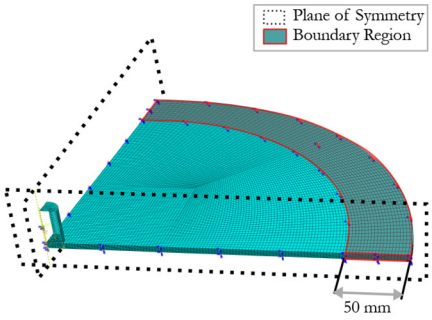


(a) Clamped circular plate with $R_0 = 250mm$ and $t = 5mm$ impacted by cylindrical impactor of $R_i = 15mm$

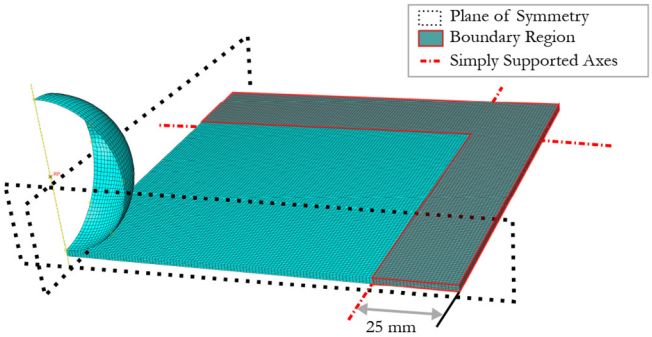


(b) Simply supported square plate with $R_0 = 100mm$ and $t = 5mm$ impacted by spherical impactor of $R_i = 25mm$

**Fig. 6.** Representation of FE model indicating the respective boundary regions and using $\chi_t = 0.5$ mm and $\chi_n = 1.0$ mm.

**Table 2**
Material properties of AA5083-H116 (Grytten et al., 2009) and Al2524 (Baptista et al., 2524; Botvina et al., 2017).

| Material | $\sigma_y$ MPa | $\sigma_u$ MPa | $\varepsilon_u$ % |
|---|---|---|---|
| AA5083-H116 | 261 | 360 | 13.1 |
| AL-2524 | 275.8 | 413.7 | 21 |

$$\varepsilon_\delta = \left|\frac{\delta_\chi - \delta_{\chi=0.5\text{mm}}}{\delta_{\chi=0.5\text{mm}}}\right| 100\% \quad \text{and}$$
$$\varepsilon_F = \left|\frac{F_\chi - F_{\chi=0.5\text{mm}}}{F_{\chi=0.5\text{mm}}}\right| 100\%. \tag{17f}$$

The left-hand side of Fig. 7a shows that both relative errors become within 1% for element size of 1.0 mm or smaller, while the computation time (CT) on the right-hand side rapidly increases. An alternative measure of convergence is the maximum artificial strain energy (AE), which should be minimised for an acceptable solution. Fig. 7b confirms that acceptable convergence is achieved with an element size 1.0 mm (i.e. $AE \leqslant 0.35\%$). The resulting mesh was shown in Fig. 6a.

### 3.3.2. Result comparison

The impact responses of the two cases are evaluated in terms of the force history and the out-of-plane deflection profile, is shown in Fig. 8 and 9 respectively. The numerically predicted out-of-plane deflection profiles are in good agreement with the reported experimental results of Fagerholt et al. (2010). Comparison of the force histories shows that the duration of impact is properly predicted, but the impact force is consistently overestimated. Note that within the experiments the plate was perforated at the highest impact velocity, whereas damage characteristics and corresponding element deletion settings have not been included in the FEM. However, the impact response is properly reproduced up to the initiation of penetration (i.e. up to 2.6 ms).

## 3.4. Verification of Metal MIDAS-M

The FE model was validated by comparing it to tests presented in Figs. 8 and 9. It can now be used as the reference to which the predictions of MIDAS-M will be compared using an aerospace-grade alloy. The comparison is performed over a range of scenarios to determine a range of confidence in which MIDAS-M can be used. The range of scenarios considered is based on dimensions of wide-

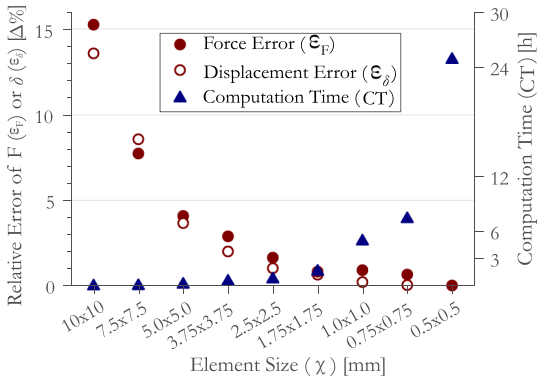


(a) (Left y-axis) Relative error of displacement/force and (Right y-axis) Computation Time versus element size

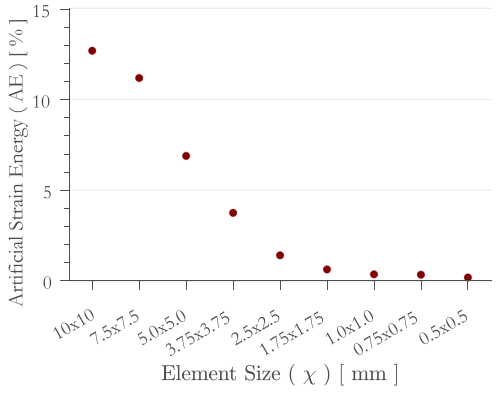


(b) Artificial strain energy as fraction of impact energy versus element size

**Fig. 7.** Mesh convergence of FEM model with respect to Fagerholt's impact scenario with a velocity of 7.31 m/s (Fagerholt et al., 2010).

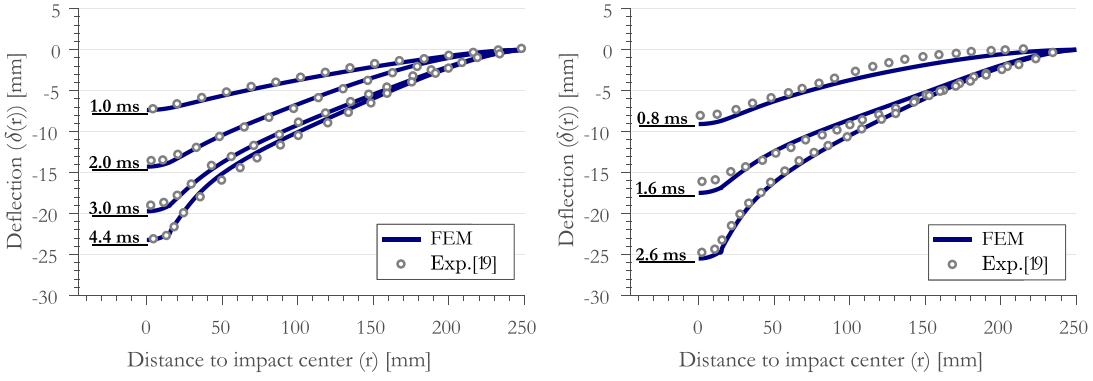


(a) $V_i = 7.31m/s$ (b) $V_i = 10.69m/s$

**Fig. 8.** Comparison of deformation profiles between the FEM and Fagerholt's experimental results at two different impact velocities (Fagerholt et al., 2010).

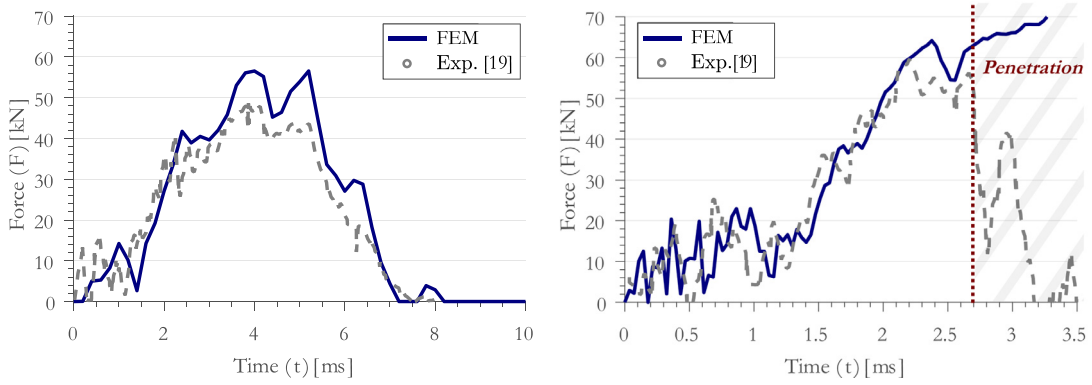


(a) $V_i = 7.31m/s$ (b) $V_i = 10.69m/s$

**Fig. 9.** Comparison of load history between the FEM and Fagerholt's experimental results at two different impact velocities (Fagerholt et al., 2010).

body aircraft. The verification of MIDAS-M is performed in two steps. The initial verification step considers the loading phase of the impact event, and the second step evaluates the permanent deformation estimates.

### 3.4.1. Reference cases for verification

The described model simplifies aircraft structures to a flat plate with a size equal to the stringer and frame pitch. An overview of fuselage designs of wide-body aircraft is given by CODAMEIN (Composite Damage Metrics and Inspection) (Haase and Mikulik, 2012). According to the CODAMEIN report, metal aircraft, such as the B777, use aluminium Al2524 as the primary material for skin, frame, and stringers. The range of fuselage dimensions and relevant material properties of aluminium Al2524 are summarised in respectively Tables 2 and 3.

The inscribed circle of the plate (i.e. the smallest side) governs the membrane behaviour of the plate. To that extent, the verification of MIDAS-M is based on square plates using the stringer pitch estimates. This work focuses on the B777 aircraft fleet, which has relatively large stringer pitch compared to the indicated range. The verification uses a plate size of 200 and 300 mm, which are the boundaries for practical scenarios. In addition, the indicated thickness range is relatively small. A thickness range of 1–4 mm is considered and impactor radii of 10, 25 and 75 mm are used.

**Table 3**
Range of wide-body aircraft fuselage dimensions (Haase and Mikulik, 2012).

| Stringer pitch mm | Frame pitch mm | Skin thickness mm |
|---|---|---|
| 150–250 | 457.2–533.4 | 1.0–2.6 |

### 3.4.2. Result comparison

The inductive solution procedure consists of a loading and unloading step. The end of loading is achieved when the specimen fully absorbs the kinetic impact energy (i.e. impactor velocity is zero). The maximum force and displacement characterise this moment. The comparison of the predicted and simulated maximum force and displacement can, therefore, be seen as an indicator of the validity of the energy conversion. Various combinations of plate and impactor dimensions are compared. These scenarios are all evaluated at four reference energy levels (5, 10, 25 and 50 J). Fig. 10a shows a comparison of three different impactor radii (10, 25 and 75 mm) on two different plates sizes (200 and 300 mm) using a constant thickness of 2 mm. Using constant plate size and impactor radius (i.e. respectively 200 mm and 25 mm), Fig. 10b compares the effect of thickness. In both figures, the predicted loading path of MIDAS-M is shown and the crosses indicated the individual case predictions at the four reference energy levels (5, 10, 25 and 50 J). The results from the FEM simulations are indicated at the same energy levels with various marker types depending on the comparison scenario.

The trends shown in both Fig. 10a and b indicate that predicted loading paths of MIDAS-M are in good agreement with the FEM simulations. The effect of changing the impactor radius, plate width or thickness is properly captured by MIDAS-M. Even though the differences increase at higher impact energies, the error

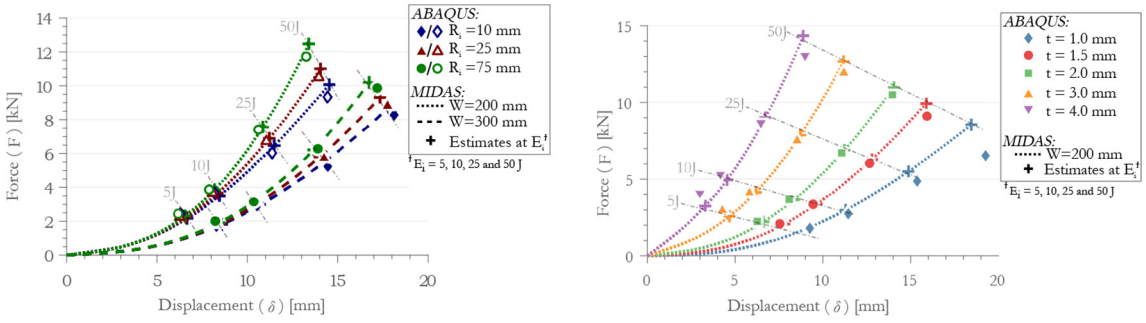


(a) Variation of impactor and plate size (b) Variation of plate thickness

**Fig. 10.** Comparison of MIDAS with FEM simulations.

remains within 10% except for plates with a thickness of 1 mm. The error of predicted force increases between impact energies of 25 and 50 J for these 1 mm plates. Investigation of the FEM results shows that this discrepancy results from excessive element distortion in the boundary region. MIDAS-M does not include this distortion, and further work is required to investigate the behaviour of thin flexible targets. The exact reason for this discrepancy for very thin plates is not clear. It is believed that the membrane and bending effects are not captured by the present model with sufficient accuracy. In addition, the extent to which the assumptions of quasi-static impact are valid for such plates should be investigated. This topic is the subject of on-going work.

In addition to the force–displacement paths, the deformation shape, contact radius and plastic limit are relevant characteristics to compare. The maximum and permanent deformations of several scenarios are compared in Figs. 11–13. Figs. 11 and 12 compare results at four energy levels for 2 mm thick and 200 mm wide plates with impactor radii of respectively 10 and 75 mm, while Fig. 13 compares the deformation shapes of different thicknesses with an impactor radius of 25 mm and impact energy 50 J. The contact radii estimates of both the FEM and MIDAS-M are approximately the same, while the validity of the deformation shape approximation varies. Effectively, it can be said that the validity of the deformation shape varies with plate thickness. Fig. 13 shows the deformation shape is not properly reproduced for thicker plates (t = 3–4 mm) compared to the estimates for thin plates (t = 1.5–2 mm). Similarly, the error in plastic radius estimates is significant for the thicker plates. The estimates for plates of 1.5–2 mm are in good agreement with FEM. The plastic range is underestimated at lower impact energies, but the differences become smaller at 25 and 50 J. Similarly, comparison of the permanent dent estimates show differences of approximately 20% around 25–50 J, while the error is larger at 5–10 J.

## 4. Application – Impactor characteristics from field data

Data collected on damage created during service of aircraft are used here to define the impact threats which may have caused it. There are two steps in the process of using damage dimensions as input to then deduce and present the calculated threats: generate a contour map of all possible damage dimensions and plot the reference data to interpolate the impactor size and energy. The deductive problem will simulate multiple events of impact on an aluminium plate to create a contour map of all possible damages. Using a sample dataset of impact damage dimensions and the contour map, the impactor radius and energy will be estimated.

The model runs simulations for multiple impactor radii (ranging from 1 mm to 250 mm) striking the aluminium plate. This produces a contour map of a wide range of impact events with their associated damage dimensions, as shown in Fig. 14. On the one hand, the simulation shows that for a fixed impactor radius more severe damage is created with increasing energy, both in terms of damage depth and radius. The simulation continues for an impactor radius until it reaches fracture limits as stated by Section 2.2.1, producing the upper bound of the contour map. On the other hand, with an increasing impactor radius and fixed energy, the damage depth decreases but the damage radius

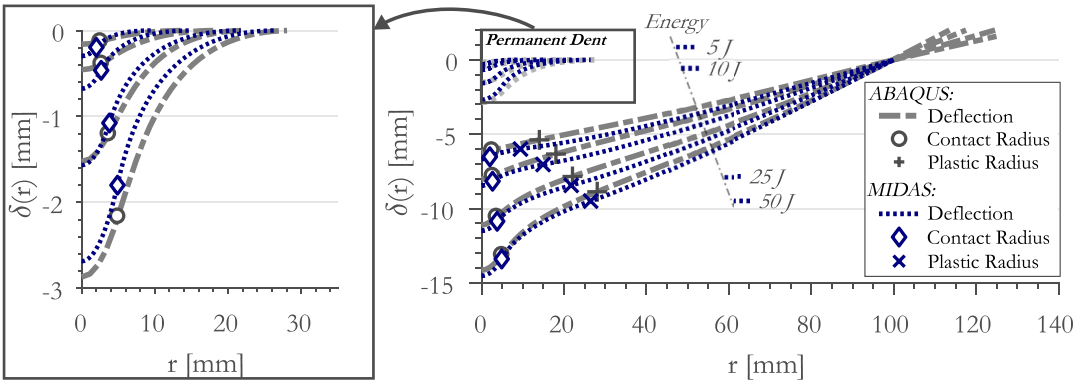


**Fig. 11.** Maximum and permanent deformation of MIDAS-M and FEM for 200 mm wide and 2 mm thick plate impacted with an impact radius of 10 mm at four impact energies (5/10/25/50 J).

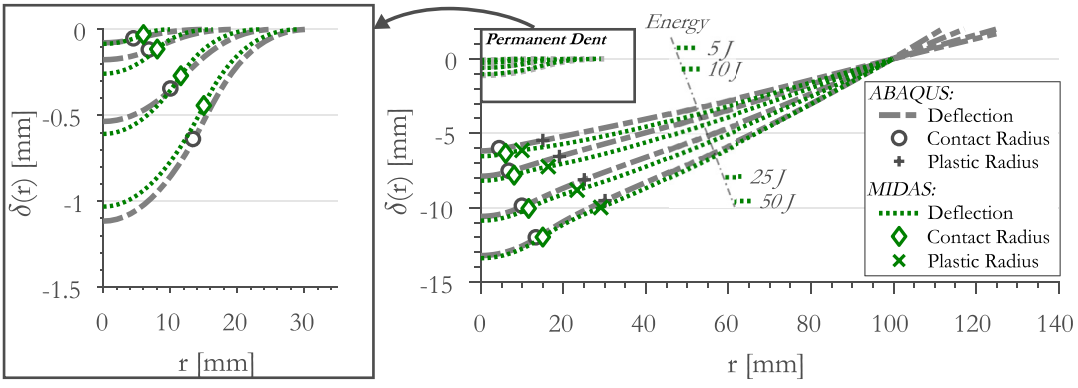


**Fig. 12.** Maximum and permanent deformation of MIDAS-M and FEM for 200 mm wide and 2 mm thick plate impacted with an impact radius of 75 mm at four impact energies (5/10/25/50 J).

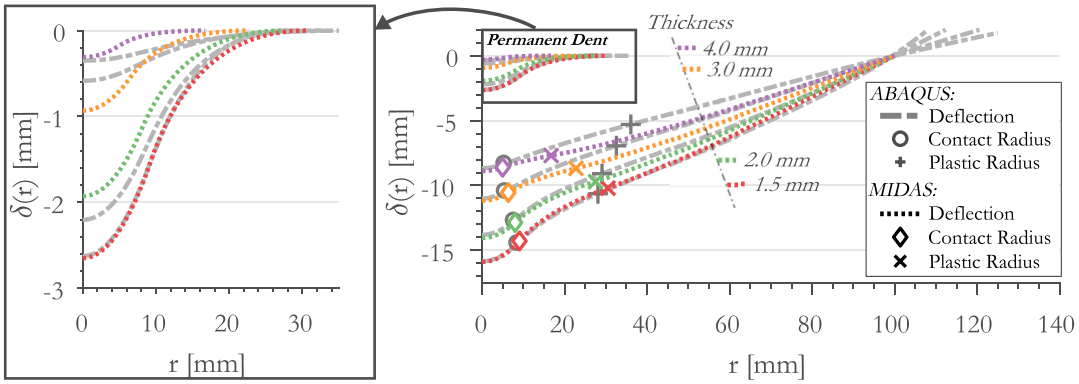


**Fig. 13.** Maximum and permanent deformation of MIDAS-M and FEM for 200 mm wide plate and varying thickness (1.5/2/3/4 mm) impacted at 50 J with an impact radius of 25 mm at an impact energy of 50 J.

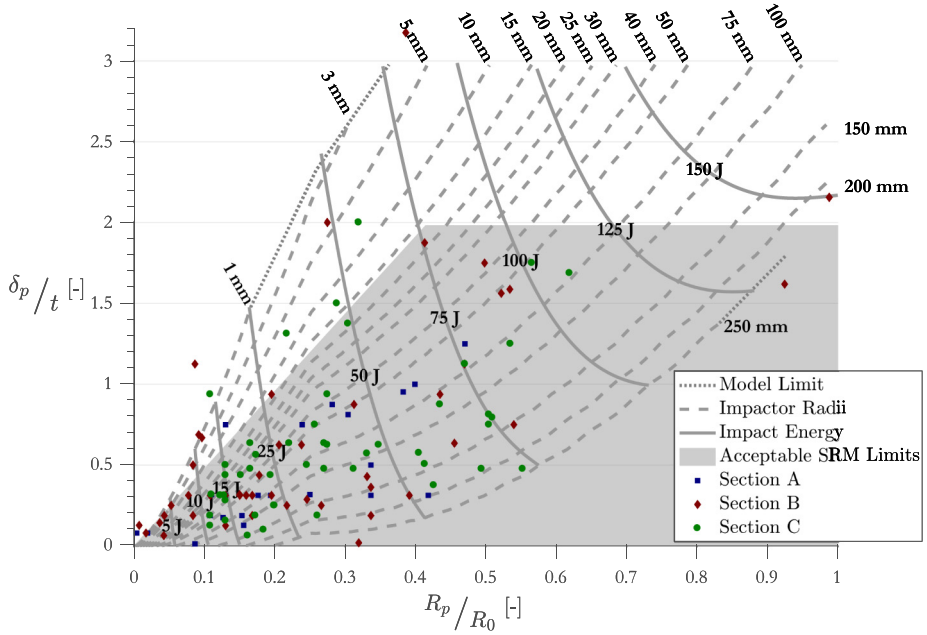


**Fig. 14.** Reference damage data superimposed on impact threat map.

increases. This trend is due to the larger contact radius between the impactor and the plate, leading to a shallower but larger damage area. The variation in the balance between impactor radii and energy generates a wide range of possible aluminium damages.

The deductive problem approach was able to interpolate the impactor radii and energy for 110 out of the 120 data points as shown in Fig. 14. The remaining data points fell out of the bounds of the contour map for impactor sizes smaller than 1 mm. At these values, MIDAS-M is at the limit of its capabilities to model a significantly small impactor.

## 5. Discussion

In the setup of developing MIDAS-M and the case study using maintenance data, key assumptions are made. These assumptions and their effect on the results are discussed in the framework of the theoretical approach presented.

Superimposing the bending and membrane deformation in MIDAS-M introduced a transition region. In the verification of MIDAS-M against the FEM model, its applicability is linked to the thickness of the plates. The limitation of the plate thickness follows from the assumed interaction of bending and membrane deformation contributions occurring in this transition region. The difference in deformation shape for the 3–4 mm thick plates can be attributed to an overestimation of the bending contribution. The maximum force estimation errors can also be significant for thinner skins (<1.5 mm) at high energies. Although this can be considered a drawback, the scatter in indentation measurements is still of the same order of magnitude. Nevertheless, to address these errors and broaden the application of the model to a wider range of plate thicknesses, the definition of the assumed state of strain of the plate should be revisited. In addition, the analysis here was carried out assuming all impacts were at the centre of the panel. This was done in order to obtain preliminary trends. In future, the effect of impacts anywhere on the panel should be accounted for.

## 6. Conclusion

The usual approach of determining the damage resulting from a certain impactor, characterised by material, size, and energy, has

been reversed to test the degree to which damage dimensions can be used to deduce and identify the source characteristics of the damage. The deductive approach captures the variability in the impact threat characteristics (size and energy).

The analytical approach, Modelling Impact Damage on Metal Aircraft Structures (MIDAS-M), is based on the combined contribution of global plate deflection theory and penetration limits. The resulting model gives maximum force predictions which are within 10% of measured results, and only for thin plates (1 mm or less) the error is, in some cases, as high as 20%. The errors in the shape of the deformation and by extension the final permanent damage dimension are more influenced by the thickness of the plate than any other factor. For highest accuracy when compared to the validated Finite Element Model, the plate thickness range of MIDAS-M applicability was determined to be 1.5–3 mm. With the range of validity in mind, the deductive approach was able to predict the impact threats of 110 out of the 120 maintenance damage dimensions. Despite some deviation, the main advantage MIDAS-M has over computational (FEM) models is the number of cases it can process in a fraction of the time it takes the computational model to calculate even a single case.

Several recommendations can be identified for MIDAS-M. Beyond the manner in which deformation theory is implemented, the range of impact scenarios for MIDAS-M can be extended. Currently, the model only considers flat plates with perpendicular impacts. However, fuselage sections can be single or double curved surfaces that have different responses to both perpendicular and oblique impacts. Accounting for these factors may also lead to modelling of elliptical damages. Additionally, the development of MIDAS-M started with the assumption of quasi-static impact, but this may not apply to certain impactor size or energies. Furthermore, adding stringer and frame interactions could allow for more accurate modelling of off-centre impacts, covering a larger area of the aircraft. Consequently, this research has indeed presented a model that is able to estimate the physical characteristics of an impactor that has caused a certain resulting damage. Therefore, one is able to infer what has caused a certain type of damage, the distribution of the damage type and severity relative to impactor types, and how to in future reduce such occurrences while also being better prepared in terms of what to expect from a given impactor source.

## Declaration of Competing Interest

The authors declare that they have no known competing financial interests or personal relationships that could have appeared to influence the work reported in this paper.

## References


Abrate, S., 1991. Impact on laminated composite materials. Appl. Mech. Rev. 44, 155. https://doi.org/10.1115/1.3119500. URL: http://appliedmechanicsreviews.asmedigitalcollection.asme.org/article.aspx?articleid=1394347.

Abrate, S., 1994. Impact on laminated composites: recent advances. Appl. Mech. Rev. 47, 517. https://doi.org/10.1115/1.3111065.

Abrate, S., 2001. Modeling of impacts on composite structures. Compos. Struct. 51, 129–138. https://doi.org/10.1016/S0263-8223(00)00138-0.

Baptista, C., Adib, A., Torres, M., Pastoukhov, V., 2524. Describing fatigue crack growth and load ratio effects in Al 2524 T3 alloy with an enhanced exponential model. Mech. Mater. 51, 66–73. https://doi.org/10.1016/j.mechmat.2012.04.003.

Big-Alabo, A., Harrison, P., Cartmell, M., 2015. Contact model for elastoplastic analysis of half-space indentation by a spherical impactor. Comput. Struct. 151, 20–29. https://doi.org/10.1016/j.compstruc.2015.01.005.

Botvina, L., Nesterenko, G., Soldatenkov, A., Demina, Y., Sviridov, A., 2017. Development of short fatigue cracks in aluminum alloy 2524–T3 specimens. Russian Metallurgy (Metally) 2017, 322–329. https://doi.org/10.1134/S0036029517040024. URL: http://link.springer.com/10.1134/S0036029517040024.

Cairns, D., Simple, A., 1991. Elasto-plastic contact law for composites. J. Reinf. Plast. Compos. 10, 423–433.

Cantwell, W., Morton, J., 1991. The impact resistance of composite materials—a review. Composites 22, 347–362.

Chen, W., Engel, P., 1972. Impact and contact stress analysis in multilayer media. Int. J. Solids Struct. 8, 1257–1281.

Chen, W., Xu, Q., Ning, H., Wang, T., Li, J., 2011. Foreign object debris surveillance network for runway security. Aircraft Eng. Aerospace Technol. 83, 229–234.

Chen, X., Ren, H., Bil, C., 2014. Inspection intervals optimization for aircraft composite structures considering dent damage. J. Aircraft 51, 303–309. https://doi.org/10.2514/1.C032377. URL: http://arc.aiaa.org/doi/10.2514/1.C032377.

Christoforou, A., 2001. Impact dynamics and damage in composite structures. Compos. Struct. 52, 181–188. https://doi.org/10.1016/S0263-8223(00)00166-5.

Christoforou, A., Yigit, A., Majeed, M., 2012. Low-velocity impact response of structures with local plastic deformation: characterization and scaling. J. Comput. Nonlinear Dyn. 8,. https://doi.org/10.1115/1.4006532. URL: http://computationalnonlinear.asmedigitalcollection.asme.org/article.aspx?doi=10.1115/1.4006532 011012.

Curran, R., Kundu, A., Raghunathan, S., McFadden, R., 2002. Impact of aerodynamic surface tolerance on aircraft cost driver. Proc. Inst. Mech. Eng., Part G: J. Aerospace Eng. 216, 29–39.

Curran, R., Kundu, A., Raghunathan, S., Eakin, D., McFadden, R., 2003. Influence of manufacturing tolerance on aircraft direct operating cost (doc). J. Mater. Process. Technol. 138, 208–213.

Curran, R., Castagne, S., Early, J., Price, M., Raghunathan, S., Butterfield, J., Gibson, A., 2007. Aircraft cost modelling using the genetic causal technique within a systems engineering approach. Aeronaut. J. 111, 409–420.

Davies, G., Olsson, R., 2004. Impact on composite structures. Aeronaut. J. 108, 541–563. https://doi.org/10.1017/S0001924000000385. URL: https://www.cambridge.org/core/product/identifier/S0001924000000385/type/journal_article.

Davies, G., Zhang, X., 1993. Impact damage prediction in carbon composite structures. Int. J. Impact Eng 16, 149–170. https://doi.org/10.1016/0734-743X(94)00039-Y.

Dhanisetty, V., Verhagen, W., Curran, R., 2017. Multi-criteria weighted decision making for operational maintenance processes. J. Air Transp. Manage. https://doi.org/10.1016/j.jairtraman.2017.09.005.

Dhanisetty, V., Massart, P., Esrail, F., Verhagen, W., Kassapoglou, C., Curran, R., 2019. Prediction of damage due to impact for composites on the basis of possible impact threats. Int. J. Impact Eng 103317.

Esrail, F., Kassapoglou, C., 2014. An efficient approach for damage quantification in quasi-isotropic composite laminates under low speed impact. Compos. Part B: Eng. 61, 116–126. https://doi.org/10.1016/j.compositesb.2014.01.033.

Fagerholt, E., Grytten, F., Gihleengen, B., Langseth, M., Børvik, T., 2010. Continuous out-of-plane deformation measurements of AA5083-H116 plates subjected to low-velocity impact loading. Int. J. Mech. Sci. 52, 689–705. https://doi.org/10.1016/j.ijmecsci.2009.11.013.

Federal Aviation Administration (FAA), Airport Foreign Object Debris (FOD) Management - AC 150/5210-24, 2010. URL: https://www.faa.gov/airports/resources/advisory_circulars/index.cfm/go/document.current/documentNumber/150_5210-24..

Grytten, F., Børvik, T., Hopperstad, O., Langseth, M., 2009. Low velocity perforation of AA5083-H116 aluminium plates. Int. J. Impact Eng 36, 597–610. https://doi.org/10.1016/j.ijimpeng.2008.09.002.

Haase, P., Mikulik, Z., 2012. Composite damage metrics and inspection, Technical Report, European Aviation Safety Agency (EASA), Hamburg. doi: EASA.2010.C13..

Honomichl, S.B., Detwiler, A.G., Smith, P.L., 2013. Observed hazards to aircraft in deep summertime convective clouds from 4–7 km. J. Aircraft 50, 926–935.

Jones, N., 2011. Structural Impact. Cambridge University Press.

Kassapoglou, C., 2013. Design and Analysis of Composite Structures: with Applications to Aerospace Structures. URL: http://ebookcentral.proquest.com/lib/ucm/detail.action?docID=1160769 http://ebookcentral.proquest.com/lib/columbia/detail.action?docID=1160769..

Langseth, M., Larsen, P., 1988. Dropped objects. plugging capacity of steel plates..

Langseth, M., Larsen, P., 1990. Dropped objects' plugging capacity of steel plates: an experimental investigation. Int. J. Impact Eng. 9, 289–316.

Langseth, M., Larsen, P., 1994. Dropped objects' plugging capacity of aluminium alloy plates. Int. J. Impact Eng. 15, 225–241.

Lee, Y., Woertz, J., Wierzbicki, T., 2004. Fracture prediction of thin plates under hemi-spherical punch with calibration and experimental verification. Int. J. Mech. Sci. 46, 751–781. https://doi.org/10.1016/j.ijmecsci.2004.05.004. URL: http://linkinghub.elsevier.com/retrieve/pii/S0020740304001079.

Liu, B., Villavicencio, R., Guedes Soares, C., 2014. On the failure criterion of aluminum and steel plates subjected to low-velocity impact by a spherical indenter. Int. J. Mech. Sci. 80, 1–15. https://doi.org/10.1016/j.ijmecsci.2013.12.015.

Martin, J., Belant, J., DeVault, T. Blackwell, B. Berger, L. Riffell, S. Wang, G., 2011. Wildlife risk to aviation: a multi-scale issue requires a multi-scale solution..

Mittal, R., 1987. A simplified analysis of the effect of transverse shear on the response of elastic plates to impact loading. Int. J. Solids Struct. 23, 1191–1203.

Mohotti, D., Ali, M., Ngo, T., Lu, J., Mendis, P., Ruan, D., 2013. Out-of-plane impact resistance of aluminium plates subjected to low velocity impacts. Mater. Des. 50, 413–426. https://doi.org/10.1016/j.matdes.2013.03.023.

Olsson, R., 2000. Mass criterion for wave controlled impact response of composite plates. Compos. Part A: Appl. Sci. Manuf. 31, 879–887. https://doi.org/10.1016/S1359-835X(00)00020-8.

Olsson, R., 2015. Analytical prediction of damage due to large mass impact on thin ply composites. Compos. Part A: Appl. Sci. Manuf. 72, 184–191. https://doi.org/10.1016/j.compositesa.2015.02.005.

Razali, N., Sultan, M., Mustapha, F., Yidris, N., Ishak, M., 2014. Impact damage on composite structures a review. Int. J. Eng. Sci. 3, 8–20.

Richardson, M., Wisheart, M., 1996. Review of low-velocity impact properties of composite materials. Compos. Part A: Appl. Sci. Manuf. 27, 1123–1131. https://doi.org/10.1016/1359-835X(96)00074-7. URL: http://linkinghub.elsevier.com/retrieve/pii/1359835X96000747.

Schonberg, W., Keer, L.M., Woo, T., 1987. Low velocity impact of transversely isotropic beams and plates. Int. J. Solids Struct. 23, 871–896.

Shivakumar, K., Elber, W., Illg, W., 1983. Prediction of impact force and duration due to low-velocity impact on circular composite laminates. J. Appl. Mech. 52, 674–680. https://doi.org/10.1115/1.3169120.

Shupikov, A., Ugrimov, S., Smetankina, N., Yareshchenko, V., Onhirsky, G., Ukolov, V., Samoylenko, V., Avramenko, V., 2012. Bird dummy for investigating the bird-strike resistance of aircraft components. J. Aircraft 50, 817–826.

Simonsen, B., Lauridsen, L., 2000. Energy absorption and ductile failure in metal sheets under lateral indentation by a sphere. Int. J. Impact Eng. 24, 1017–1039. https://doi.org/10.1016/S0734-743X(00)00024-5.

Singh, H., Mahajan, P., 2016. Analytical modeling of low velocity large mass impact on composite plate including damage evolution. Compos. Struct. 149, 79–92. https://doi.org/10.1016/j.compstruct.2016.04.009.

Soldatini, C., Georgalas, V., Torricelli, P., Albores-Barajas, Y., 2010. An ecological approach to birdstrike risk analysis. Eur. J. Wildl. Res. 56, 623–632.

Systèmes, Dassault, 2013. ABAQUS Documentation, 6.13 ed., Providence, RI, USA. URL: http://abaqus.software.polimi.it/v6.13/index.html..

Swanson, Stephen R, 1992. Limits of Quasi-Static Solutions in Impact of Composite Structures. Composites Engineering 2, 261–267. https://doi.org/10.1016/0961-9526(92)90009-U. In press.

Taylor, R., Govindjee, S., 2002. Solution of Clamped Rectangular Plate Problems Technical Report. University of California, Berkeley.

Yigit, A., Christoforou, A., 2007. Limits of asymptotic solutions in low-velocity impact of composite plates. Compos. Struct. 81, 568–574. https://doi.org/10.1016/j.compstruct.2006.10.006.